

Shapes and dynamic regimes of an active fluid droplet under confinement

Adriano Tiribocchi^{1*}, Mihir Durve² and Marco Lauricella¹ Andrea Montessori³ Davide Marenduzzo⁴ Sauro Succi^{1,2,5}

1 Istituto per le Applicazioni del Calcolo CNR, via dei Taurini 19, 00185 Rome, Italy

2 Center for Life Nano Science@La Sapienza, Istituto Italiano di Tecnologia, 00161 Roma, Italy

3 Department of Engineering, Roma Tre University, Via Vito Volterra 62, 00146 Rome, Italy

4 Scottish Universities Physics Alliance, School of Physics and Astronomy, University of Edinburgh, Edinburgh EH9 3JZ, United Kingdom

5 Department of Physics, Harvard University, Cambridge, MA, 02138, USA

* adrianotiribocchi@gmail.com

August 18, 2022

Abstract

Active droplets are artificial microswimmers built from a liquid dispersion by microfluidic tools and showing self-propelled motion. These systems hold particular interest for mimicking biological phenomena, such as some aspects of cell locomotion and collective behaviors of bacterial colonies, as well as for the design of droplet-based biologically inspired materials, such as engineered tissues. Growing evidence suggests that geometrical confinement crucially affects their morphology and motility, but the driving physical mechanisms are still poorly understood. Here we study the effect of activity on a droplet containing a contractile fluid confined within microfluidic channels of various sizes. We find a surprising wealth of shapes and dynamic regimes, whose mechanics is regulated by a subtle interplay between contractile stress, droplet elasticity and microchannel width. They range from worm-like and fish-like shaped droplets displaying an oscillating behavior within wider channels to bullet-shaped droplets exhibiting rectilinear motion in narrower slits. Our findings support the view that geometrical confinement can provide a viable strategy to control and predict the propulsion direction of active droplets. It would be of interest to look for analogues of these motility modes in biological cells or in synthetic active matter.

Contents

1	Introduction	2
2	METHODS	4
2.1	Free energy	4
2.2	Equations of motion	4
2.3	Numerical implementation and mapping to physical units	5

3	Results	6
3.1	Contractile droplet in an unbounded passive fluid	6
3.2	Weak confinement	8
3.3	Intermediate confinement	11
3.4	Strong confinement	12
3.5	Shape deformations and variations of the liquid crystal orientation	14
3.6	Phase diagram	15
4	Conclusions	17
	References	19

1 Introduction

Active matter comprises systems in which the constituents building-blocks are capable of continuously converting chemical energy into mechanical work [1, 2]. An important paradigm of active matter are fluids of self propelled rod-like units with the tendency to assemble, giving rise to liquid crystals with nematic or polar order [3]. Instances of these hierarchical soft structures (often termed active gels [4]) are ubiquitous in nature and range from bacterial or algae suspensions [5, 6] to mixtures of cytoskeletal filaments (such as actin or microtubules) and molecular motors [7]. The interaction of these internal entities with each other and with the surrounding medium produces mechanical stress causing a surprising number of non-equilibrium effects, such as collective motion at large scales [8–10], spontaneous flows [11, 12], turbulence at low Reynolds number [13, 14] and exotic rheological responses [15–17]. This instability ultimately depends upon the nature of the forces generated by the active particles, whether they are contractile (pulling fluid inwards longitudinally and emitting it perpendicularly) or extensile (vice versa).

Recent microfluidic advances have shown that the self-locomotion of micrometer-sized fluid droplets can be enabled by encapsulating an active gel within an emulsified dispersion of oil in water. Successful experimental realizations include, for example, stabilized bundles of microtubules cross-linked by kinesin (an extensile gel) adsorbed onto the interface of a droplet [11, 18] or included at its interior [19], and acto-myosin fibres (contractile gel) assembled within cell-sized droplets [20]. Besides their biological importance as model tools to study complex biological processes, such as intracellular movements [1, 21], cell swimming [22] and crawling [23, 24], they may be ideal candidates for the design of bio-inspired active materials potentially useful in material science, for the assemble of engineered tissues from cell layers [25, 26], and in pharmaceuticals as microreactors for cargo delivery, including drug delivery and water remediation [27–30].

Under these circumstances, these self-motile droplets often navigate within confined microenvironments (such as porous viscoelastic tissues and capillary vessels), a situation that poses additional constraints, with respect to unconfined systems, to their morphology and locomotion regimes, especially in the presence of narrow interstices [31, 32]. Indeed, the presence of confining interfaces (or walls) can decisively affect the swimming motion due to unavoi-

able disturbances of the hydrodynamic flow field which could ultimately impact on droplet shape and stability. Such physiological-like conditions can be partially reproduced in *in-vitro* experiments by means of suitable microfluidic devices in which an active droplet migrates within micrometer-sized channels in a controlled manner [20, 28, 33–37]. While a large body of studies have been focused on investigating the physics of weakly confined swimmers [38–43], much less is known in highly confined geometries despite their practical relevance.

In this paper, we numerically study the dynamics of a polar active fluid droplet navigating within microchannels of various heights whose design draws inspiration from real microfluidic devices [35, 37]. The framework to understand the physics of this system is provided by the hydrodynamic theory of active gels [1, 4] in which a scalar field $\phi(\mathbf{r}, t)$, accounting for the density of the active material, and a liquid crystal vector field $\mathbf{P}(\mathbf{r}, t)$, capturing its orientational order, are governed by advection-relaxation equations while a further field $\mathbf{v}(\mathbf{r}, t)$, defining the global fluid velocity, obeys the Navier-Stokes equation. The active forces triggering the droplet self propulsion are included, via an active stress, in the pressure tensor, whose passive part stems from functional differentiation of a Landau-de Gennes free energy (more details are given in the section 2).

Extensive lattice Boltzmann simulations show a striking variety of shapes and dynamic regimes whose formation relies upon a delicate balance between contractile stress, droplet elasticity and degree of confinement (defined as the ratio between height of the channel and droplet diameter). While, under weak confinement, the droplet is generally found to exhibit an oscillatory self propelled motion with shapes ranging from a rounded cell-like structure at small active doping to a stretched worm-like configuration at large activity, increasing the confinement considerably impacts on shapes and droplet trajectories. At intermediate confinement, the droplet attains a fish-like shape at high active stress (a less distorted structure than the previous one) and shows, once again, a unidirectional motion with persistent oscillations whereas, at small activity, oscillations become negligible and the droplet assumes a bullet-like profile. Further increasing the confinement prevents the droplet motion, except for cases in which a high active stress fosters recurrent and periodic shape changes without producing any net displacement. The dynamical behaviour we find is richer than the one observed for confined squirmers [44, 45], which can also entail sustained oscillations, because of the key role played by both shape deformations and internal fluid flow in our droplets, which are absent in squirmers.

The motility regimes found here are characterized in terms of the structure of the flow field, and of its coupling with the orientation of the active material and the droplet interface. The fluid velocity, in particular, displays a pair of counter-rotating vortices during the rectilinear motion and a single vortex as the droplet navigates close to a wall, while the polar liquid crystal generally acquires splay deformations of higher strengths at larger activities. Shape changes and variation of the orientation of the liquid crystal are quantitatively assessed in terms of elastic free energy changes associated with droplet interface and liquid crystal distortions. All these findings are finally summarised in a phase diagram providing an overview of the dynamics of a contractile fluid droplet swimming in microfluidic channels.

The paper is structured as follows. In the next section we shortly describe the hydrodynamic gel theory alongside some numerical aspects concerning the simulation setup. Afterwards we illustrate the numerical results, initially focusing on the dynamics of the active droplet in an unbounded medium and then on that within microchannels of various heights. A selection of shapes and motility regimes are discussed in three different confinement conditions, together with quantitative measurements of center of mass position and speed, as well

as of elastic free energy. The aforementioned phase diagram and some final remarks close the paper.

2 METHODS

2.1 Free energy

The physics of a polar active fluid droplet immersed in a passive Newtonian fluid can be described in terms of the following set of coarse-grained fields: (i) $\phi(\mathbf{r}, t)$, the concentration of the active material; (ii) $\mathbf{P}(\mathbf{r}, t)$ the polarization of the liquid crystal; (iii) $\rho(\mathbf{r}, t)$ and (iv) $\mathbf{u}(\mathbf{r}, t)$, respectively mass density and velocity field of the fluid. Our active droplet is designed as a circular region comprising a contractile gel ($\phi > 0$, $\mathbf{P} \neq 0$), which can be experimental realized, for example, with bundles of actin filaments cross-linked with myosin motor protein [1, 46]. This suspension is surrounded by a passive wet solvent ($\phi = 0$ and $\mathbf{P} = 0$) confined between two parallel flat walls, whose geometry is inspired by a real microfluidic channel.

The equilibrium properties of the passive limit of this suspension are encoded in the following free energy density [47, 48]

$$f = \frac{a}{4\phi_{cr}^4} \phi^2 (\phi - \phi_0)^2 + \frac{k}{2} (\nabla \phi)^2 - \frac{\alpha (\phi - \phi_{cr})}{2 \phi_{cr}} |\mathbf{P}|^2 + \frac{\alpha}{4} |\mathbf{P}|^4 + \frac{\kappa}{2} (\nabla \mathbf{P})^2, \quad (1)$$

where the first two terms describe bulk and interfacial properties of a binary fluid mixture while the remaining ones capture those of the polar liquid crystal. More specifically, the first term of Eq.1 multiplied by the positive constant a guarantees the separation of the binary fluid into two components, $\phi = \phi_0$ (with ϕ_0 approximately equal to 2) inside the droplet and $\phi = 0$ outside. The second terms controls the interfacial tension of the drop, which is given by $\sigma = \sqrt{8ak/9}$ where k and a are positive constants. The terms multiplied by the constant α represent the bulk contributions associated with the liquid crystal phase and $\phi_{cr} = \phi_0/2$ is the critical concentration controlling the transition from the isotropic phase (outside the active drop) to the polar one (within the drop). Finally, the term in gradients of \mathbf{P} accounts for the local deformations of the liquid crystal within the standard approximation of the single elastic constant κ [49].

To summarize, at equilibrium we have the following phases minimizing the free energy $\mathcal{F} = \int_V f dV$: a polar active phase located within the drop (where $\phi = \phi_0$ and $\mathbf{P} = \mathbf{P}_{eq}$) and a passive isotropic one (where $\phi = 0$ and $\mathbf{P} = 0$) outside; across the interface of the droplet, ϕ and \mathbf{P} vary smoothly from $\phi = \phi_0$ and $\mathbf{P} = \mathbf{P}_{eq}$ to $\phi = 0$ and $\mathbf{P} = 0$.

2.2 Equations of motion

The fluid velocity \mathbf{v} is governed by the Navier-Stokes equations which, in the incompressible limit, read

$$\nabla \cdot \mathbf{v} = 0, \quad (2)$$

$$\rho \left(\frac{\partial}{\partial t} + \mathbf{u} \cdot \nabla \right) \mathbf{u} = -\nabla p + \nabla \cdot (\underline{\underline{\sigma}}^{active} + \underline{\underline{\sigma}}^{passive}). \quad (3)$$

Here ρ is the density of the fluid and p is the isotropic pressure. In the right hand side, $\underline{\underline{\sigma}}^{active} + \underline{\underline{\sigma}}^{passive}$ is the total stress tensor, given by the sum of active and passive terms. The

former is [2]

$$\sigma_{\alpha\beta}^{active} = -\zeta\phi \left(P_\alpha P_\beta - \frac{1}{2}|\mathbf{P}|^2\delta_{\alpha\beta} \right), \quad (4)$$

where Greek indexes denote Cartesian components and ζ is the activity, which is positive for extensile particles and negative for contractile ones [1]. In our simulations it is kept negative, meaning that the active gel contracts along the direction of the inner units.

The passive stress comprises three further contributions, namely a viscous term $\sigma_{\alpha\beta}^{viscous} = \eta(\partial_\alpha v_\beta + \partial_\beta v_\alpha)$ where η is the shear viscosity, an elastic stress $\underline{\underline{\sigma}}^{elastic}$ due to bulk distortions of the liquid crystal and a surface tension term $\underline{\underline{\sigma}}^{interface}$. The elastic contribution is

$$\sigma_{\alpha\beta}^{elastic} = \frac{1}{2}(P_\alpha h_\beta - P_\beta h_\alpha) - \frac{\xi}{2}(P_\alpha h_\beta + P_\beta h_\alpha) - \kappa\partial_\alpha P_\gamma\partial_\beta P_\gamma, \quad (5)$$

while the interfacial one is

$$\sigma_{\alpha\beta}^{interface} = \left[\left(f - \phi \frac{\delta\mathcal{F}}{\delta\phi} \right) \delta_{\alpha\beta} - \frac{\partial f}{\partial(\partial_\beta\phi)} \partial_\alpha\phi \right]. \quad (6)$$

The dynamics of the order parameters ϕ obeys a Cahn-Hilliard equation [50, 51]

$$\frac{\partial\phi}{\partial t} + \nabla \cdot (\phi\mathbf{u}) = M\nabla^2\mu, \quad (7)$$

where M is the mobility – chosen to be constant for simplicity – and $\mu = \delta F/\delta\phi$ is the chemical potential.

Finally, the evolution equation for the polarization $\mathbf{P}(\mathbf{r}, t)$ is given by [1]

$$\frac{\partial\mathbf{P}}{\partial t} + (\mathbf{u} \cdot \nabla)\mathbf{P} = -\underline{\underline{\Omega}} \cdot \mathbf{P} + \xi\underline{\underline{D}} \cdot \mathbf{P} - \frac{1}{\Gamma} \frac{\delta F}{\delta\mathbf{P}}, \quad (8)$$

where $\underline{\underline{D}} = (\underline{\underline{W}} + \underline{\underline{W}}^T)/2$ and $\underline{\underline{\Omega}} = (\underline{\underline{W}} - \underline{\underline{W}}^T)/2$ are the symmetric and antisymmetric part of the velocity gradient tensor $W_{\alpha\beta} = \partial_\beta u_\alpha$. The constant ξ controls the geometry of the active particles, positive for the rod-like ones and negative for disk-like ones. In addition, it determines the response of the liquid crystal under shear, which is either flow aligning (if $|\xi| > 1$) or flow tumbling (if $|\xi| < 1$). As in previous works [22, 23], we set $\xi > 1$. The last term, multiplied by the rotational viscosity Γ , is the molecular field $\mathbf{h} = \delta F/\delta\mathbf{P}$ which governs the relaxation dynamics of the liquid crystal.

2.3 Numerical implementation and mapping to physical units

Following previous studies [22, 52], Eqs.(2)-(3)-(7)-(8) are solved via a hybrid lattice Boltzmann approach [52, 53], in which a standard LB method is used for Eqs. (2) and (3) and a finite difference scheme for Eqs. (7) and (8). In particular, finite difference operators are computed using a stencil representation, an approach guaranteeing the necessary isotropy with the underlying two dimensional lattice [54, 55]. The simulations are performed on rectangular meshes, in which the horizontal direction is kept constant at $L_y = 500$ lattice sites, while the vertical one L_z is varied between 45 and 135 lattice sites. Periodic boundary conditions are set along the y -axis and two parallel flat walls are positioned at $z = 0$ and $z = L_z$. Here we impose no wetting for ϕ (i.e. $\phi|_{z=0, L_z} = 0$) and no-slip conditions for \mathbf{u} (i.e. $u|_{z=0, L_z} = 0$), while no specific anchoring is set for \mathbf{P} at the walls. In this microfluidic channel we place a contractile

droplet initialized as a circular region of radius R where $\phi(\mathbf{r}, 0) \simeq 2$ and $\mathbf{P}(\mathbf{r}, 0) = \mathbf{P}_y(\mathbf{r}, 0)$ (with $|\mathbf{P}_y| = 1$) for $r \leq R$, while $\phi(\mathbf{r}, 0) \simeq 0$ and $\mathbf{P}(\mathbf{r}, 0) = 0$ outside, for $r > R$. In our runs we have kept R constant and equal to 45 lattice sites, thus the confinement parameter $\lambda = L_z/2R$ ranges from 0.5 (which we refer to as high confinement) to 1.5 (which we refer to as low confinement).

If not stated otherwise, the thermodynamic parameters have been fixed to the following values: $a = 0.04$, $k = 0.06$, $\alpha = 0.1$, $\kappa = 0.04$, $M = 0.1$, $\xi = 1.1$, $\Gamma = 1$, $\eta \simeq 1.67$. The first two values, in particular, determine the surface tension $\sigma = \sqrt{8ak/9} \simeq 0.045$ and the interface width $\delta = 2\sqrt{2k/a} \simeq 3.5$. Also, lattice spacing and integration timestep are set to $\Delta x = 1$ and $\Delta t = 1$. Finally, the contractile activity $|\zeta|$ has been varied approximately between 5×10^{-4} and 2.5×10^{-3} : these values generally ensure a spontaneous motion while minimizing the chance to breakups, events more likely to occur in the presence of intense flows.

Simulation parameters can be mapped onto real physical units fixing length, time and force scales to the following values: $L = 1\mu\text{m}$, the time scale $T = 10\text{ms}$ and the force scale $F = 100\text{nN}$ (in simulation units these scales are equal to one) [22, 23]. Thus our system would approximately simulate a microfluidic channel of length $\sim 0.5\text{mm}$ in which the active fluid droplet of diameter $D \simeq 90\mu\text{m}$ has shear viscosity $\eta \simeq 1.5\text{kPa}\cdot\text{s}$, while the liquid crystal has effective elastic constant $\kappa \simeq 0.04\text{nN}$ and rotational viscosity $\Gamma \simeq 1\text{kPa}\cdot\text{s}$. Also, the diffusion coefficient is $D = Ma \simeq 0.4\mu\text{m}^2/\text{s}$. Finally, the speed v of the droplet in our simulation varies between $\sim 10^{-4}$ to $\sim 10^{-3}$, values roughly corresponding to $0.1 - 1\mu\text{m}/\text{s}$. These numbers ensure that the Reynolds number $Re = \rho v D / \eta$ remains equal to or lower than 0.1 and the Capillary number $Ca = v\eta/\sigma$ is below 0.1.

3 Results

We start off by describing the typical dynamics observed in an unbounded system and then we present a selection of shapes and dynamic regimes observed in the weak ($\lambda > 1$), intermediate ($\lambda \simeq 1$) and strong ($\lambda < 1$) confinement for various ζ focusing, in particular, on the fluid-structure interaction. We finally provide a full phase diagram of a contractile fluid droplet moving within microchannels of various heights.

3.1 Contractile droplet in an unbounded passive fluid

The mechanism leading to the autonomous motion of a contractile fluid droplet has been extensively studied, for example, in Refs. [22, 56]. In Fig.1 we shortly outline the physics in unbounded systems and in a regime in which the motion is unidirectional (see also movie M1). The droplet is initialized as a passive circular region in which \mathbf{P} is uniform and aligned along the y direction (Fig.1a). Then ζ is turned on and is set to a value triggering spontaneous motion. However, before this occurs, the contractile stress (whose strength is controlled by ζ) sets a four-roll mill flow which stretches the droplet longitudinally without causing any net motion (Fig.1b,f). This state results from the temporary balance between interfacial tension and elasticity of the liquid crystal, which hinder shape deformations, and contractility favouring hydrodynamic instability. Afterwards, the contractile stress overcomes the resistance to deformations mediated by liquid crystal and fluid interface and destabilizes the polarization pattern, yielding an outward splay pattern associated with the formation of two

counter-rotating vortices in the flow field, which trigger droplet motion (Fig.1c,g). Concomitantly, the droplet acquires a temporary crescent shape along the direction of motion. At late times, the droplet shape becomes rounded (Fig.1d) and the motion proceeds at constant speed parallel to the y direction (Fig.1e), sustained by the two fluid vortices (Fig.1h).

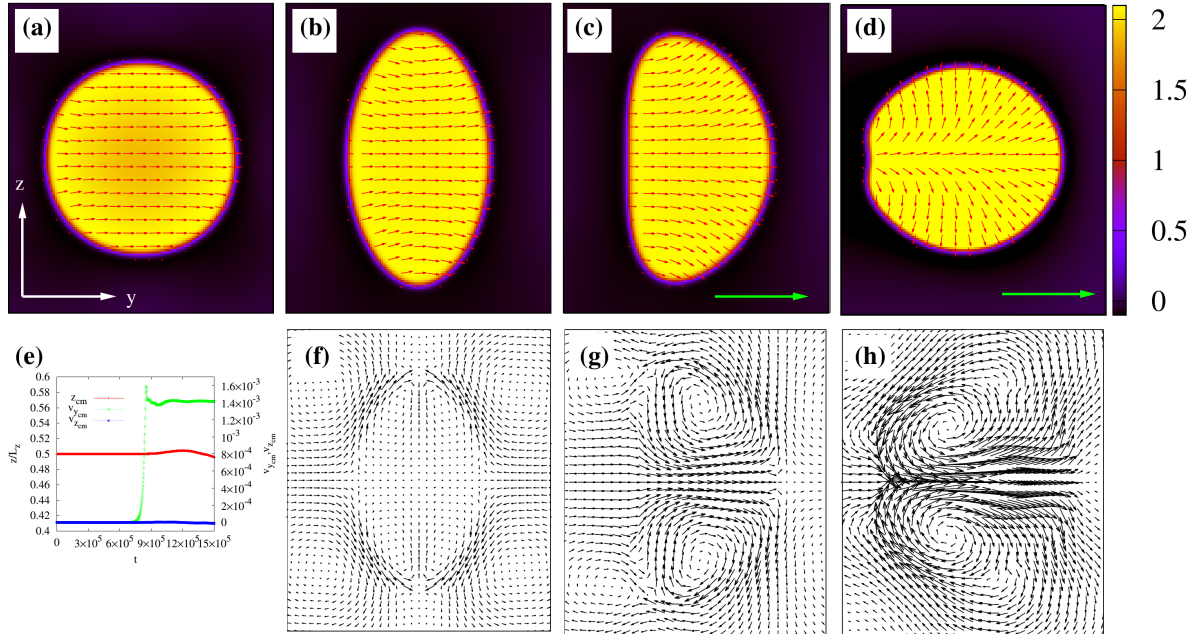


Figure 1: **Onset of autonomous motion of an active fluid droplet in an unbounded passive Newtonian fluid for $\zeta = -8 \times 10^{-4}$.** (a) Initial configuration of an equilibrated passive droplet and of the polarization, which is almost everywhere parallel to the y direction. (b)-(f) Once the activity is turned on, the droplet temporarily elongates perpendicularly to \mathbf{P} due to the contractile activity and its associated four-vortex fluid flow pattern, which pulls the fluid along the equator of the droplet and expels it longitudinally. (c)-(g) Afterwards, the uniform polarization becomes unstable with respect to splay deformations. This instability is due to the large contractile stress which favours the spontaneous formation of two counter-rotating vortices triggering the motion of the droplet. (d)-(h) The droplet acquires a stable rounded shape and moves unidirectionally sustained by the two internal vortices. The color bar ranges from $\phi \simeq 0$ (black) to $\phi \simeq 2$ (yellow), red arrows represent the direction of the polarization \mathbf{P} and the green arrow indicates the direction of motion. Black arrows shows the local direction of the velocity field \mathbf{v} . This applies to all figures. (e) Time evolution of the z component of the center of mass (left axis) and of y and z components of its speed (right axis).

Increasing $|\zeta|$ generally leads to higher order instabilities in which one observes, unlike the previous case, the concurrent presence of regions where neighboring vectors of \mathbf{P} splay outwards ($\nabla \cdot \mathbf{P} > 0$) and inwards ($\nabla \cdot \mathbf{P} < 0$). In Fig.2 (and movie M2) we show, for example, the onset of spontaneous motion of an active droplet with $\zeta = -10^{-3}$. Once again, the droplet initially stretches longitudinally due to the four-vortex fluid flow (Fig.2a-f) and is subsequently destabilized by the contractile stress. However, here the polarization shows three different patterns, i.e. it remains basically uniform in the middle of the droplet, where

a large counterclockwise vortex emerges, and splays inwards and outwards at the extremities, where two small clockwise vortices appear (Fig.2b-g) [57]. This fluid recirculation triggers a temporary rotation of the droplet, until the large vortex gradually merges with a small one into a large double-vortex structure (Fig.2c-h and d-i), finally yielding a unidirectional motion (Fig.2 e-j). In this configuration, the polarization exhibits a single inward splay distortion spanning the whole droplet.

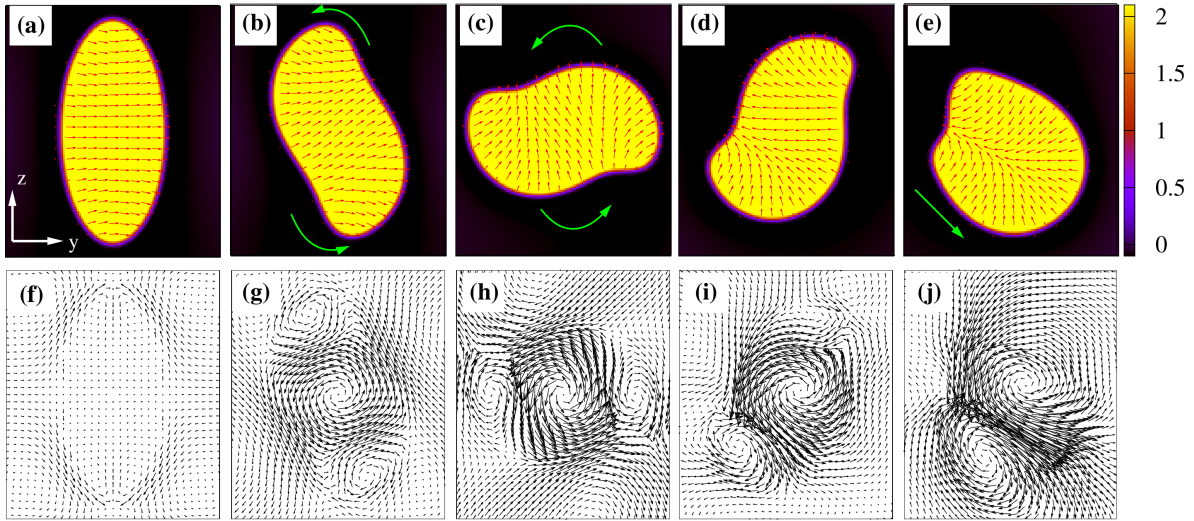


Figure 2: **Onset of instability in an active fluid droplet in an unbounded passive Newtonian fluid for $\zeta = -10^{-3}$.** Once the activity is turned on, the fluid flow stretches the droplet longitudinally (a-f). Then the contractile stress destabilizes the polarization, which remains uniform in the bulk of the droplet and splays at the extremities (b-g). Three contiguous fluid vortices, a large one rotating counterclockwise and two others rotating clockwise, emerge and trigger the rotation of the droplet (c-h). Afterwards, the large vortex in the middle and the small one on the top merge into a large double-vortex structure leading to self propulsion, while the polarization progressively rearranges to yield a single splay deformation pointing inwards (d-i and e-j).

These results suggest that, although at the onset of the instability the dynamic features (shape, structure of polarization and velocity field) depend on ζ , in the steady state the droplet is essentially found to move along a rectilinear path without relevant perturbations, for a wide range of values of active parameter (see also movie M3 for $\zeta = -1.5 \times 10^{-3}$). In the next section we show that, under confinement, this picture is dramatically altered and the active droplet displays a multifarious range of shapes and dynamic regimes which are absent in unbounded systems.

3.2 Weak confinement

In Fig.3 we show the active droplet dynamics for $\lambda \simeq 1.5$ and $\zeta = -1.5 \times 10^{-3}$ (see also movie M4 for the full dynamics). The onset of the instability resembles the one observed in unconfined systems: the droplet initially stretches longitudinally due to the four-roll mill flow only mildly affecting the orientation of the polarization field (Fig.3a,g). Afterwards, the

contractile stress deforms the droplet, which displays two temporary symmetric branches. Here the polarization splay outwards at the front, where a couple of counter-rotating fluid vortices emerges, and inwards at the rear, where two smaller vortices form (Fig.3b,h). These ones then merge with the leading ones giving rise to two large fluid recirculating patterns pushing the droplet forward (Fig.3c,i). In this configuration, the droplet attains a slightly elongated shape and the polar field globally shows an outward splay distortion. However, the presence of the walls crucially alters the perfect symmetry of the vortices, an effect that modifies droplet shape and orientation of the polarization finally causing a deviation from the rectilinear trajectory. Indeed, a weak perturbation of the droplet position (caused by the interaction between fluid and walls) may drive, for example, the droplet downwards near the bottom wall (Fig.3d,j). Here, the fluid vortex in the vicinity of the wall lessens while the one far from it strengthens, thus allowing the droplet to turn towards the middle of the channel (where the double vortex structures is temporarily restored, Fig.3e,k). Once in close contact with the top wall, the droplet weakly flattens and turns downwards driven, once again, by a single vortex, now rotating clockwise (Fig.3f,l). During this process, its shape remains globally akin to that observed in the short rectilinear motion of Fig.3c, while the polarization shows a long-lasting splay deformation pointing outwards and parallel to the direction of locomotion. Such dynamics repeats itself, giving rise to a regular and persistent oscillatory behavior in which the droplet moves forward periodically hitting opposite walls (see also Fig.5, where the position of center of mass and its speed are plotted).

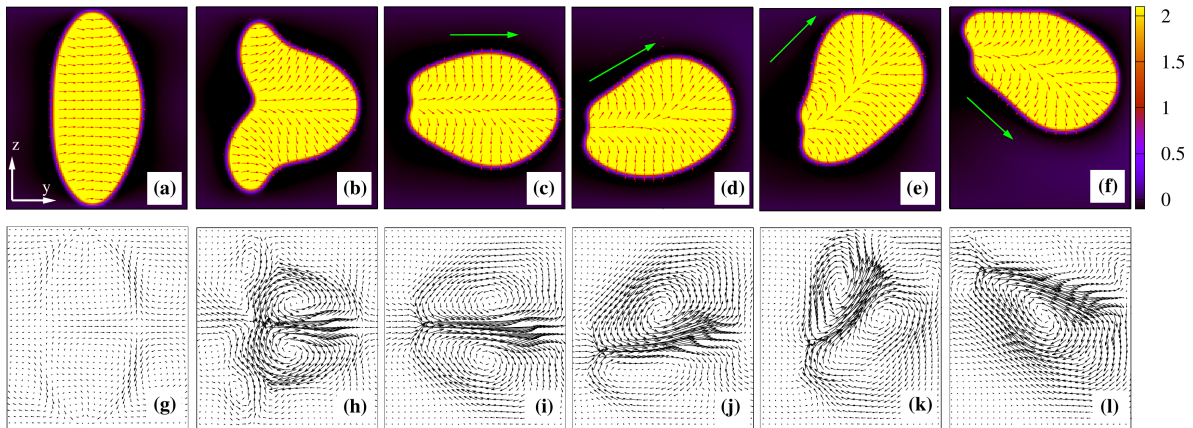


Figure 3: Shapes and dynamic behavior of an active fluid droplet with $\zeta = -1.5 \times 10^{-3}$ and $\lambda \simeq 1.5$. Once ζ is turned on, the droplet stretches longitudinally (a) due to the usual four-vortex structure of the fluid in its surrounding (g). Afterwards, the contractile stress destabilizes this configuration, favouring the formation of two roughly symmetric branches in which the polar field gives rise to splay deformations, pointing outwards at the front of the droplet and inwards at its rear (b). Alongside the two large counter-rotating vortices, two short-lived small ones emerge on the back (h). The droplet then acquires a slightly elongated cell-like shape (c) self propelled by the usual double-vortex velocity field (i). As the droplet moves downwards and approaches the wall (d), the vortex at the bottom weakens (j), an effect that reverses the motion towards the upper wall (e,k). Finally, the droplet hits the top wall and turns downwards, once again driven by a single fluid vortex surviving far from the boundary (f,l).

For stronger contractile stresses, the droplet undergoes higher shape deformations albeit the essential features of the periodic motion are preserved. In Fig.4 (and movie M5) we show the dynamics of the active droplet for $\lambda \simeq 1.5$ and $\zeta = -2.5 \times 10^{-3}$. The onset of the instability occurs through steps akin to the previous case, i.e. a vertical elongation with uniform polarization caused by the four-vortex flow (Fig.4a,g) and a subsequent double tail deformation with symmetric splay distortions of the polar field, an arrangement due to a couple of neighboring counter-rotating vortices placed at the front plus two separate smaller ones located at the rear (Fig.4b,h). Afterwards, the larger contractile stress significantly affects morphology and dynamics of the droplet. Indeed, the two tails merge leading to a wormlike shaped droplet, whose propulsion is sustained by a combination of an intense stream crossing the drop midsection plus highly stretched fluid vortices located on both sides (Fig.4c,i). Once again, the complex interaction between active medium and surrounding fluid with the microchannel destabilizes the rectilinear motion, giving rise to a periodic dynamics in which the droplet proceeds forward but regularly hitting against both walls. The droplet initially turns downwards (Fig.4d,j) and, once near the wall, glides over it, driven by a large unidirectional stream which is, in turn, flanked by stretched vortices continuously breaking and reforming (Fig.4e,k). Afterwards, as in the case of lower contractility, the fluid vortex near the bottom wall dramatically weakens, thus allowing the droplet to turn and move towards the upper wall (Fig.4f,l). During such process, the polar field essentially preserves a large splay deformation pointing outwards and parallel to the direction of motion.

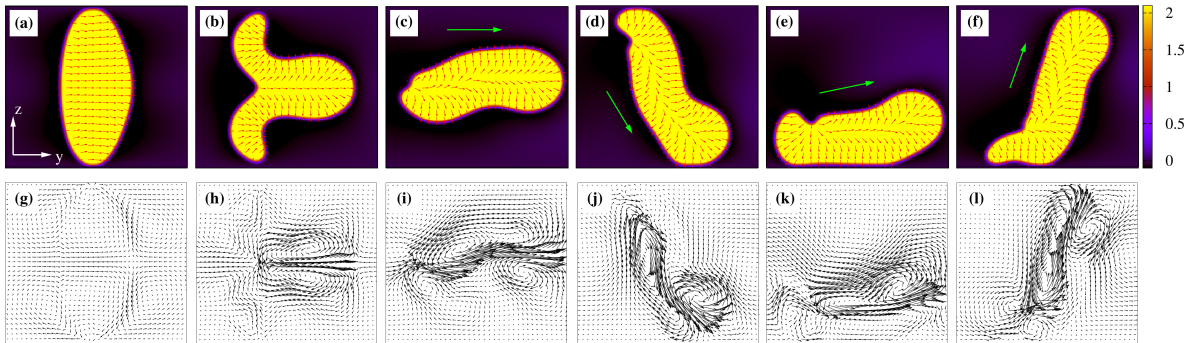


Figure 4: **Shapes and dynamic behavior of an active fluid droplet with $\zeta = -2.5 \times 10^{-3}$ and $\lambda \simeq 1.5$.** Once again, the contractile stress destabilizes the droplet, which stretches longitudinally (with a uniform polarization) (a) and then lengthens horizontally acquiring a marked bifurcation at the rear (b) (with a global splay deformation of the polarization). Here the velocity field turns to a stretched double vortex (h) from an initial four-roll pattern (g). Afterwards, the two branches merge and the droplet temporarily moves forward (c), propelled by a large single stream supported by smaller fluid vortices on both sides (i). As in the previous case, the interaction of the fluid with the walls destabilizes the rectilinear motion favouring an oscillatory dynamics where a highly elongated worm-like droplet moves towards the bottom wall (d), glides over it (e) and turns upwards to opposite wall (f). Such motion is mainly guided by a stream crossing the droplet longitudinally, while side vortices of various size continuously break and reform (j,k,l).

These simulations show that, under confinement, increasing the active stress yields two crucial features: morphologically, it favours larger shape deformations becoming permanent

at late times; dynamically, it fosters a persistent periodic dynamics characterized by a regular oscillatory motion of the droplet.

Such behavior can be quantitatively captured by tracking position and speed of the center of mass of the droplet, as shown in Fig.5. While at low values of $|\zeta|$ they display only mild oscillations, at higher values their amplitude and frequency increase, an effect caused by the stronger flows produced by the higher contractility. Note, in particular, that $v_{y_{cm}}$ attains a local maximum when the droplet glides over the walls (top or bottom) and turns (downwards or upwards), while a local minimum is found when the droplet hits the wall almost perpendicularly (Fig.5d,e,f,g). On the contrary, $v_{z_{cm}}$ achieves the largest values when the drop, slightly after the collision with the wall, starts to glide over it, while it rapidly diminishes and becomes almost negligible when the drop remains in close contact with the walls (Fig.5h,i,j,k).

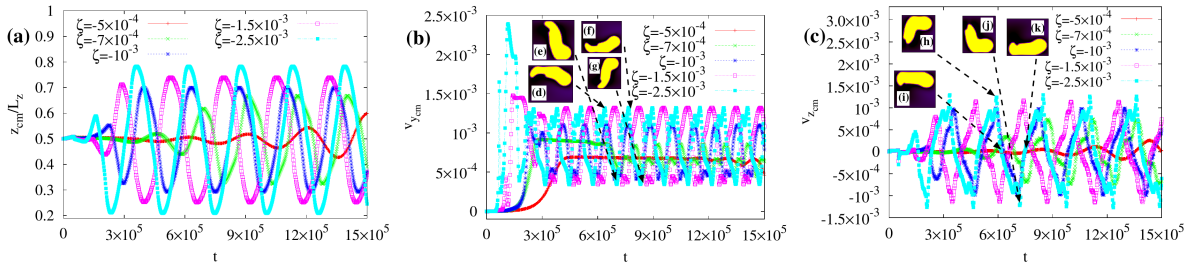


Figure 5: Position and speed of the droplet center of mass under weak confinement. (a) Time evolution of the z -component of the center of mass of the droplet for various values of activity. Increasing $|\zeta|$ augments both the amplitude and frequency of oscillations. (b)-(c). Time evolution of y and z components of the speed of the center of mass. The snapshots represent instantaneous configurations of the droplet for $\zeta = -2.5 \times 10^{-3}$ when $v_{y_{cm}}$ has a local maximum (d,f) and a local minimum (e,g), and when $v_{z_{cm}}$ has a local maximum (h), is approximately zero (i,k) and has a local minimum (j).

3.3 Intermediate confinement

Increasing the confinement parameter λ gives rise to further shapes and dynamic regimes. In Fig.6 (and movie M6) we show an active droplet swimming within a microfluidic channel with $\lambda \simeq 1$ and $\zeta = -2 \times 10^{-3}$. Under these conditions, the fluid interface of an initially static droplet slightly flattens near the walls due to the absence of wetting. Once the activity is switched on, the contractile stress produces the usual four-vortex flow which, later on, turns into a double vortex pattern guiding the motion of a fish-like shaped droplet along the positive y -direction (Fig.6a,b,c,g,h,i). However the rectilinear trajectory lasts for a short period of time and is finally replaced by an oscillating one in which the droplet moves forward periodically hitting against the walls (see also Fig.8), following a dynamics akin to that observed for larger values of λ . Indeed, the droplet approaches the bottom wall and then migrates upwards, driven by a large frontal vortex (located far from the wall) and a weak one (near the wall) which are basically used as a steering wheel and allow the turn. Alongside these fluid vortices, a large stream of flow crossing the droplet midsection guarantees the propulsion (Fig.6d,e,f,j,k,l). In this system $v_{y_{cm}}$ attains its maximum roughly in the middle of the channel (after the drop detaches from the wall) where $v_{z_{cm}}$ is approximately null, whereas the minimum values occur

when the droplet bumps against the wall, where v_{zcm} has its largest (absolute) values (see Fig.8). Note, finally, that the amplitude of the oscillations of v_{zcm} is considerably smaller than the one observed in the low confinement regime (for similar values of ζ), essentially because the shorter height of the microchannel prevents the droplet from attaining a higher transversal speed. This is also in agreement with experimental results discussed in Ref. [37], where the behavior of self-propelled droplets confined in micro-capillary devices of different cross-sections is investigated.

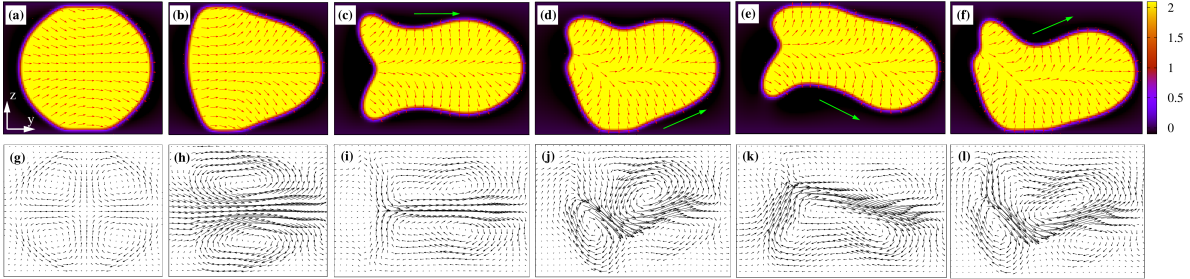


Figure 6: **Shapes and dynamic behavior of an active fluid droplet with $\zeta = -2 \times 10^{-3}$ and $\lambda \simeq 1$.** The droplet, initially squeezed within the microchannel (a), stretches horizontally (b) and moves forward with a temporary fish-like shape (c). The polarization goes from a roughly uniform pattern to a distorted one exhibiting splay deformations, while the velocity field from a four-vortex structure (h) to the usual double-vortex one (i,j). Afterwards, the droplet displays an oscillatory dynamics caused by a mechanism akin to the one described for larger values of λ . It deviates from the rectilinear trajectory, moves downwards hitting against the bottom wall (d) and then turns upwards, periodically bouncing the upper (e) and the lower wall again (f). The velocity field generally consists of a large stream located in the droplet midsection sustained by a couple of stretched counter-rotating vortices, each of which weakens near the wall (k,l,m).

If the active stress diminishes, the droplet generally undergoes milder shape deformations due to the weakening of the spontaneous flow, an effect that concurrently determines a decrease in the amplitude of oscillations of position and speed (see Fig.8) and stabilizes the motion. Such dynamics is shown in Fig.7 (and movie M7) where the contractility (here $\zeta = -1.25 \times 10^{-3}$) favours the formation of a bullet-like shaped droplet propelled along the negative y axis with negligible oscillations (see also Fig.8). The direction of motion is controlled by the usual counter-rotating double vortex which, in this case, favours an inward splay deformation of the polarization.

In the next section we will show that, in contrast to dynamic behaviors discussed so far, in a strong confinement regime the active droplet either displays an oscillating stationary dynamics without an appreciable displacement or stays altogether motionless.

3.4 Strong confinement

As an example of dynamics under strong confinement, in Fig.9 (and movies M8) we show the behavior obtained for $\zeta = -2.25 \times 10^{-3}$ and $\lambda \simeq 0.6$. A highly squeezed droplet, initially placed in the middle of the microchannel, elongates producing two separate bulges which are pushed along opposite directions by couples of counter-rotating fluid vortices. (Fig.9a,b,f,g). These,

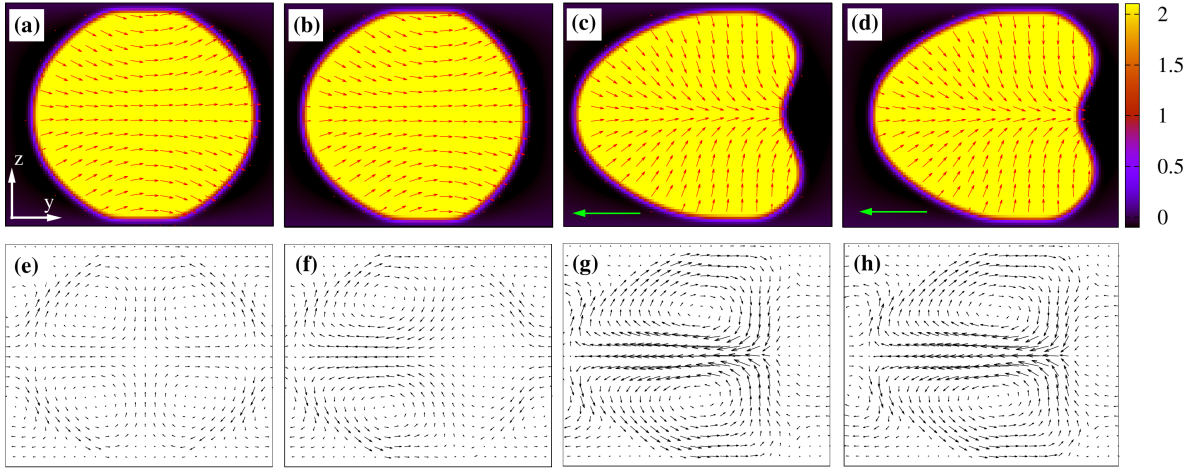


Figure 7: **Shapes and dynamic behavior of an active fluid droplet with $\zeta = -1.25 \times 10^{-3}$ and $\lambda \simeq 1$.** Once again, the contractility destabilizes the squeezed droplet (a,b) which acquires motion along the y -direction attaining a projectile shape at the steady state (c,d). The four-roll fluid velocity, observed for the non-motile droplet, gradually turns into the typical double vortex structure (f,g,h), which propels the droplet forward. Note that, in the steady state, the polarization splay inwards rather than outwards.

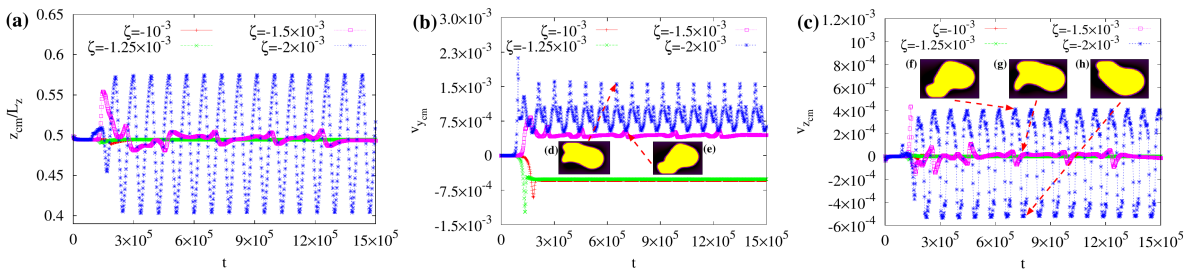


Figure 8: **Position and speed of the droplet center of mass under intermediate confinement.** (a) Time evolution of the z -component of the center of mass of the active droplet for various values of ζ and $\lambda \simeq 1$. (b)-(c). Time evolution of y and z components of the speed of the center of mass. The snapshots represent instantaneous configurations of the droplet for $\zeta = -2 \times 10^{-3}$ when $v_{y,cm}$ has local maximum (d) and a local minimum (e), and when $v_{z,cm}$ has a local maximum (f), is approximately zero (g) and has a local minimum (h).

in turn, favour the formation of splay distortions of the liquid crystal, pointing outwards at the front and inwards at the rear. The fluid protuberances continuously merge and reform due to the competition between contractile stress (which tends to destabilize the drop) and the elasticity of droplet and liquid crystal (which oppose shape deformations), until the former overcomes the latter. When this occurs, the droplet undergoes a profound reshaping in which it initially expands uniformly due to the merging of the vortices into a single large recirculating pattern (Fig.9c,h), and then it gradually acquires a temporary S-like shape. Here three smaller vortices emerge, one in the middle and two at the extremities of the drop (Fig.5d,e,i,j). The contractile stress destabilizes, once again, this state finally leading to a steady-state oscillatory behavior between S-like shaped droplets mirroring each other. In these configurations, the liquid crystal exhibits the usual splay deformation, pointing outwards where the local curvature of the interface is positive and inwards where negative.

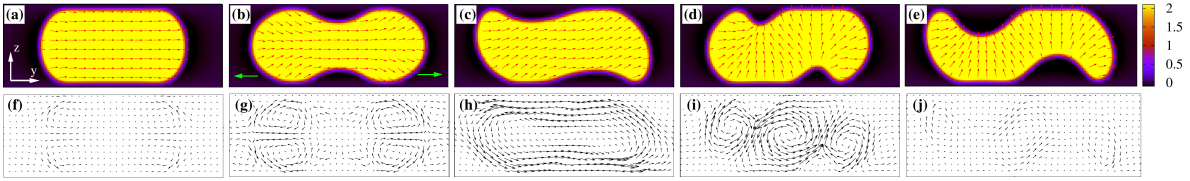


Figure 9: **Shapes and dynamic behavior of an active fluid droplet with $\zeta = -2.25 \times 10^{-3}$ and $\lambda \simeq 0.6$.** The contractile stress destabilizes a highly confined droplet which stretches and acquires a temporary dumbbell-like configuration, made of two protuberances propelled along opposite directions by two separate couples of counter-rotating vortices (a,b,f,g). Afterwards, the droplet gradually acquires an S-like shape, sustained by a large recirculating flow pattern which later on splits into three smaller vortices (c,d,e,h,i,j). The polar field shows the usual splay deformation which, in the S-shaped drop, points outwards where the interface curvature is positive and inwards where it is negative.

If $|\zeta|$ decreases, shape oscillations are suppressed. This is shown in movie M9, obtained for $\zeta = -10^{-3}$ and $\lambda \simeq 0.7$. Here the contractile stress is not sufficient to trigger any relevant change of liquid crystal orientation and shape of the droplet, which undergoes only a weak deformation due to internal feeble fluid recirculations.

3.5 Shape deformations and variations of the liquid crystal orientation

The results discussed so far point to a picture where the observed range of shapes and dynamic regimes emerge from a subtle interplay between active stress, elasticity of the drop (including that of the liquid crystal and of the interface) and confining conditions.

A more quantitative evaluation of morphological changes and variations of the liquid crystal orientation in these regimes can be obtained by monitoring the elastic free energy of the fluid interface $\mathcal{F}_{el}^{int} = \int_V k/2(\nabla\phi)^2 dV$ and that of the liquid crystal $\mathcal{F}_{el}^{lc} = \int_V \kappa/2(\nabla\mathbf{P})^2 dV$. Although these quantities only give a coarse-grained description of such modifications, their tracking over time provides a direct link with speed variations of the droplet and with the structure of the fluid velocity of the mixture. In Fig.10 we plot the time evolution of \mathcal{F}_{el}^{int} and \mathcal{F}_{el}^{lc} for $\lambda \simeq 1.5$ (top row), $\lambda \simeq 1$ (middle row), $\lambda \simeq 0.7$ (bottom row) and different values of ζ . If the contractile stress is augmented, both \mathcal{F}_{el}^{int} and \mathcal{F}_{el}^{lc} show a systematic increase, an indication that shape modifications and liquid crystal distortions become larger. More

specifically, in a larger channel (top row) high shape deformations and relevant liquid crystal distortions (maxima of Fig.10a,b) occur when the droplet crosses the channel moving towards the opposite wall (with increasing transversal speed and decreasing longitudinal one, see for example Fig.5b,c), whereas they lessen (minima of Fig.10a,b) as the droplet, after hitting the walls, retracts and then glides over it (here the longitudinal speed increases while the transversal one is negligible). These results are essentially consistent with the fact that the spontaneous flow weakens near the wall, thus the droplet would naturally tend to acquire a more rounded shape and the liquid crystal to orient more uniformly. For intermediate values of λ (Fig.10 middle row) the previous picture, i.e. larger shape deformations and higher liquid crystal distortions in the bulk rather than near the walls, basically holds although, under these conditions, such a distinction becomes slightly more elusive since droplet collisions against the walls become more frequent due to the reduced height of the microchannel.

Note finally that, at low and intermediate values of λ , the free energies display recurring oscillations of increasing amplitude, a behavior overall akin to that observed for position and speed of the droplet. On the contrary, under strong confinement oscillations become negligible since the droplet either moves unidirectionally without appreciable shape changes at the steady state or stays motionless (unless stationary oscillations emerge, such as those described in Fig.9).

3.6 Phase diagram

The complex dynamic scenario previously illustrated can be summarized in the phase diagram of Fig.11, obtained by varying $|\zeta|$ and λ .

For $\lambda \lesssim 0.7$ (strong confinement) and $|\zeta| < 1.25 \times 10^{-3}$ the highly squeezed droplet stays at rest, essentially because the contractile stress is too weak to deform the liquid crystal and the droplet interface in order to induce any net motion. On the contrary, for increasing values of $|\zeta|$ the spontaneous flow becomes high enough to trigger a unidirectional motion of the droplet which acquires, in the steady state, a bullet-like shape, a structure closely resembling that of a passive fluid droplet subject to a pressure-driven flow [48]. Further increasing $|\zeta|$ may either determine the formation of long-lasting and periodic shape oscillations without motility or occasional droplet breakups caused by intense fluid flows.

For $0.8 \lesssim \lambda \lesssim 1.2$ (intermediate confinement) the bullet shaped droplet moving along a rectilinear trajectory becomes the dominating regime at low/intermediate values of contractile activity, whereas the non-motile regime gradually shrinks towards very low values of $|\zeta|$. This occurs because, in larger channels, the constraining effect of the walls becomes progressively milder than that produced within narrower channels, thus morphological deformations and modifications of liquid crystal orientation can be more easily induced by an equally intense spontaneous flow. Alongside these dynamic regimes, two further ones emerges for increasing $|\zeta|$. For $1.5 \times 10^{-3} \lesssim |\zeta| \lesssim 2 \times 10^{-3}$, at late times the droplet is found to display a unidirectional oscillating motion with a shape resembling that of a swimming fish. As discussed in the previous sections, such dynamics results from a complex fluid-structure interaction in which the presence of the walls alters the symmetric double-vortex structure of the fluid velocity, an effect that simultaneously fosters considerable changes of shape and orientation of the liquid crystal. This is particularly relevant for a high contractile stress, since the spontaneous flow is expected to impact deeper on the droplet dynamics. Indeed, at higher values of $|\zeta|$ the motion exhibits, once again, oscillatory features but the droplet attains a highly stretched worm-like shape moving at a larger speed.

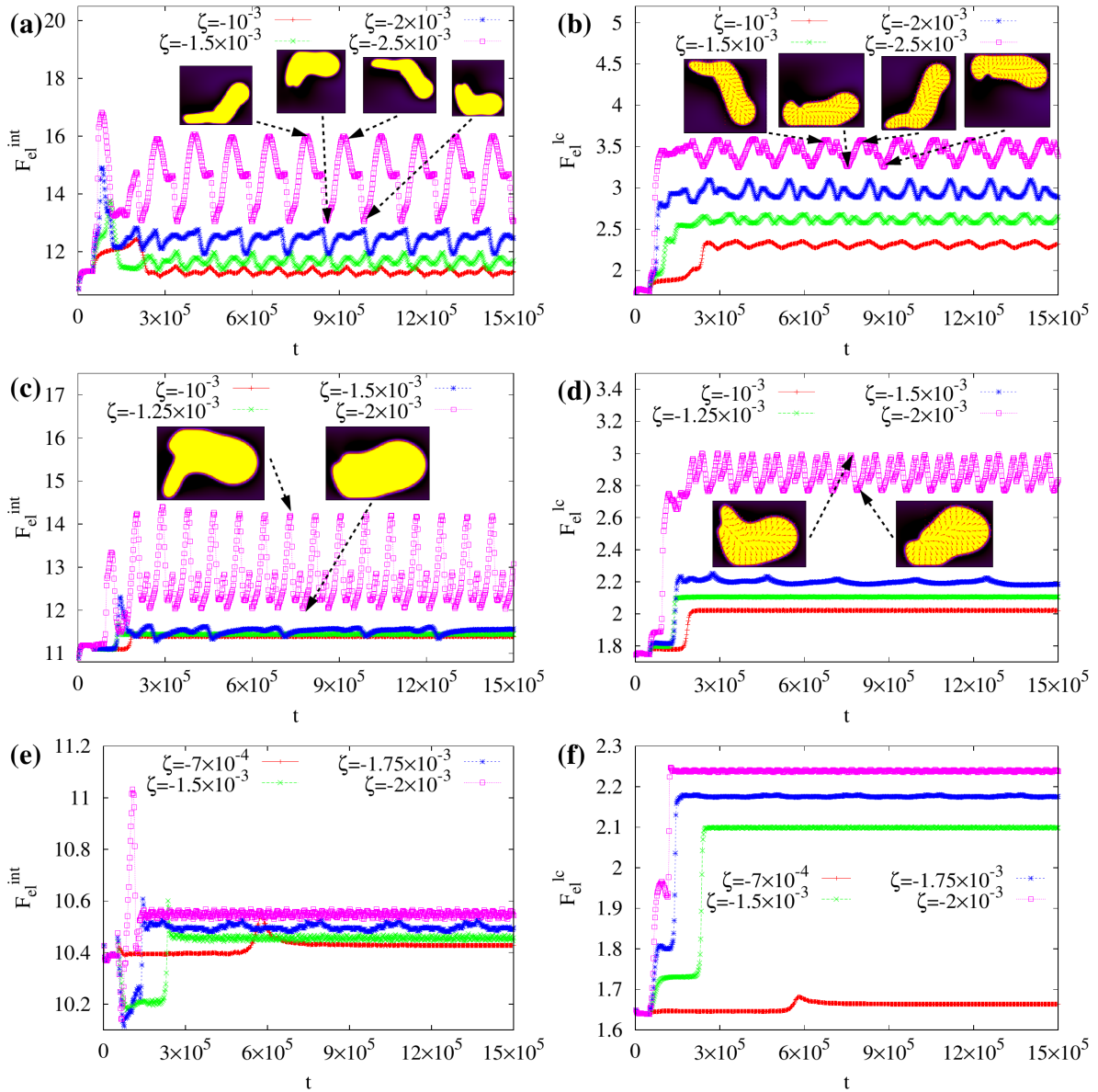


Figure 10: **Elastic free energy of the droplet.** Time evolution of $F_{el}^{int} = \int_V k/2(\nabla\phi)^2 dV$ (left column) and $F_{el}^{lc} = \int_V \kappa/2(\nabla\mathbf{P})^2 dV$ (right column) for various ζ and for $\lambda \simeq 1.5$ (a,b), $\lambda \simeq 1$ (c,d) and $\lambda \simeq 0.7$ (e,f). The insets show instantaneous configurations of ϕ and \mathbf{P} at local maxima and minima for $\zeta = -2.5 \times 10^{-3}$ (a,b) and $\zeta = -2 \times 10^{-3}$ (c,d). While at low and intermediate values of λ the free energies show long-lasting oscillations for a sufficiently large contractile stress, at high λ these oscillations are essentially suppressed, regardless of the strength of the contractility.

Finally, for $\lambda \gtrsim 1.3$, the droplet is generally found to display a periodic dynamics for roughly all values of $|\zeta|$ explored in our simulations. However, while for $|\zeta| \gtrsim 1.5 \times 10^{-3}$ the drop attains, at the steady state, the worm-like shape previously mentioned, for smaller values of $|\zeta|$ a weaker flow field mitigate the deformations, yielding a shape now resembling that of a rounded cell (i.e., the shape is akin to the one observed in unconfined systems).

4 Conclusions

In conclusion, we have numerically studied the dynamics of a polar active fluid droplet migrating within microchannels of different heights, in which the setup mimics conditions reproducible in microfluidic experiments. Our droplet comprises a contractile gel, representing a fluid containing force dipoles with long-range orientational order, confined by interfacial tension and immersed in a passive Newtonian fluid. At the walls of the channel we set no-slip conditions for the fluid velocity and no wetting for the fluid interface.

We have shown that, under confinement, the droplet displays a wealth of shapes and non-trivial dynamic behaviors resulting from a subtle interplay between active stress, droplet elasticity and fluid-structure interactions. We approximately identify six different dynamic regimes observed under weak, intermediate and strong confinement, characterized by peculiar morphological features and distinctive motility conditions. Under weak confinement the droplet exhibits a unidirectional oscillatory motion acquiring, at the steady state, either a cell-like shape (for low/intermediate active stress) or an elongated worm-like structure (for large active stress). Dialling up the degree of confinement, morphological changes during the motion generally diminish, and the droplet shows either a periodic dynamics with a fish-like shape or an oscillation-free rectilinear motion with a bullet-like profile. Under high confinement, motility is overall suppressed except for large contractile mixtures. On a general basis, a periodic behavior alongside with considerable shape deformations emerge when the degree of confinement remains intermediate/low and the contractility is intermediate/high, otherwise the droplet shows simpler dynamic features. The formation of such striking variety of shapes and the associated motility regimes crucially depend upon the structure of the fluid velocity which, during the oscillatory motion, exhibits two main patterns: i) a couple of counter-rotating vortices if the droplet moves far from the walls and ii) a single vortex with a large stream crossing the drop midsection if the motion occurs near the walls. The former is generally the typical structure observed in self-propelled droplets moving along a predefined direction while the latter allows the droplet to turn and detach from the walls. Under high confinement, where oscillations are generally negligible due to the lack of sufficient space, a net displacement would be solely triggered by the double vortex fluid.

Active droplets, like the ones described in this work, may be realized using water-oil emulsions including a contractile material, such as the actomyosin protein complex found in the cytoskeleton of living cells [20]. Indeed, these active droplets have been previously shown to capture some aspects of cell locomotion, such as swimming in an unbounded fluid [22, 58] and crawling on a solid substrate [23], albeit they remain distant from a real cell [24]. Nonetheless, their simplified architecture could provide a robust platform for the manufacturing of biomimetic synthetic swimmers with the propensity to move. In this respect our results, besides being useful for a deeper understanding the physics of these objects, also suggest that their direction of self-locomotion can be more easily controlled and predicted when they move

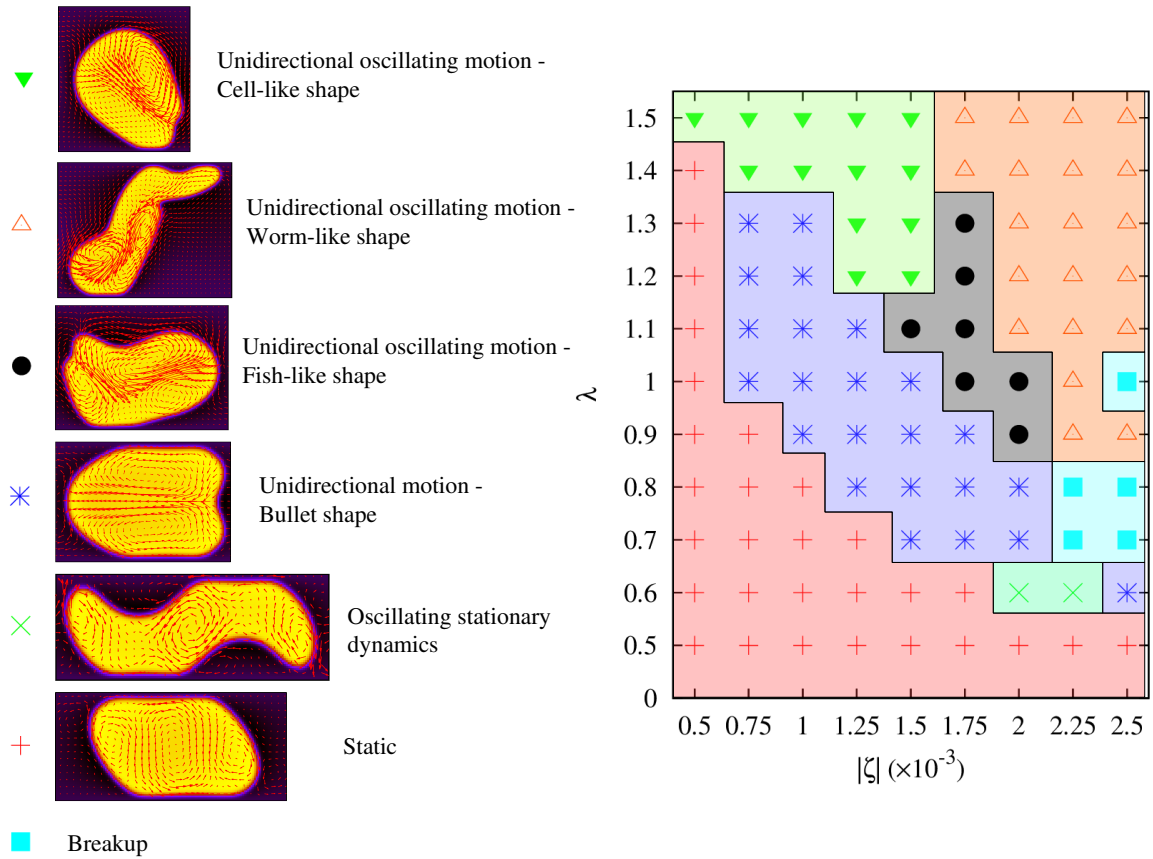


Figure 11: **Phase diagram of an active droplet for different values of confinement parameter $\lambda = L_z/D$ and activity ζ .** Left: Selection of shapes of a contractile fluid droplet moving within microchannels of various height. Red arrows show the velocity field within the droplet and in its surrounding. Right: Under strong confinement ($\lambda \lesssim 0.7$), for low values of $|\zeta|$ the droplet remains static (red/plus), while for high values of $|\zeta|$ it either displays stationary oscillations (green/cross) or acquires a bullet-like shape (blue/asterisk) moving unidirectionally. Also, occasional breakups (light blue/square) occur for very high values of $|\zeta|$. Under intermediate confinement ($0.8 \lesssim \lambda \lesssim 1.2$), the droplet exhibits a larger variety of shapes and dynamic regimes, ranging from fish-like (black/circle) and cell-like (green/triangle) structures for intermediate values of $|\zeta|$ to a worm-like (orange/triangle) geometry for higher values. In all such cases the droplet moves unidirectionally and displays a persistent oscillatory dynamics. At lower values of $|\zeta|$, the droplet shows, once again, a bullet shape moving without oscillations or remains motionless. Under weak confinement ($\lambda \gtrsim 1.3$), droplets self propel with long-lasting oscillations while their shapes mainly range from cell-like ones for lower $|\zeta|$ to stretched worm-like ones (orange/triangle) for higher $|\zeta|$.

within suitable confined environments (such as those whose design is inspired to physiological environments), a scenario particularly relevant in several technological applications, ranging from drug delivery to the design of soft composite materials. It would be finally of interest to perform a fully 3D study to see how spatial dimensionality may affect shape and dynamic behavior of the droplet.

Supplementary Material

List of movies

Movie M1: This movie shows the active droplet dynamics swimming in an unbounded medium for $\zeta = -8 \times 10^{-4}$.

Movie M2: This movie shows the active droplet dynamics swimming in an unbounded medium for $\zeta = -10^{-3}$.

Movie M3: This movie shows the active droplet dynamics swimming in an unbounded medium for $\zeta = -1.5 \times 10^{-3}$.

Movie M4: This movie shows the active droplet dynamics for $\lambda \simeq 1.5$ and $\zeta = -1.5 \times 10^{-3}$.

Movie M5: This movie shows the active droplet dynamics for $\lambda \simeq 1.5$ and $\zeta = -2.5 \times 10^{-3}$.

Movie M6: This movie shows the active droplet dynamics for $\lambda \simeq 1$ and $\zeta = -2 \times 10^{-3}$.

Movie M7: This movie shows the active droplet dynamics for $\lambda \simeq 1$ and $\zeta = -1.25 \times 10^{-3}$.

Movie M8: This movie shows the active droplet dynamics for $\lambda \simeq 0.6$ and $\zeta = -2.25 \times 10^{-3}$.

Movie M9: This movie shows the active droplet dynamics for $\lambda \simeq 0.7$ and $\zeta = -10^{-3}$.

Acknowledgments

A. T., M. D., M. L., A. M. and S. S. acknowledge funding from the European Research Council under the European Union's Horizon 2020 Framework Programme (No. FP/2014-2020) ERC Grant Agreement No.739964 (COPMAT).

References

- [1] M. C. Marchetti, J. F. Joanny, T. Ramaswamy, T. B. Liverpool, J. Prost, M. Rao and R. Aditi Simha, *Hydrodynamics of soft active matter*, Rev. Mod. Phys. **85**, 1143 (2013), doi:<https://doi.org/10.1103/RevModPhys.85.1143>.

- [2] R. A. Simha and S. Ramaswamy, *Hydrodynamic fluctuations and instabilities in ordered suspensions of self-propelled particles*, Phys. Rev. Lett. **89**, 058101 (2002), doi:<https://doi.org/10.1103/PhysRevLett.89.058101>.
- [3] A. Majumdar, M. C. Marchetti and E. G. Virga, *Perspectives in active liquid crystals*, Phil. Trans. R. Soc. A **372**, 20130373 (2014), doi:<https://doi.org/10.1098/rsta.2013.0373>.
- [4] J. Prost, F. Jülicher and J. F. Joanny, *Active gel physics*, Nature Physics **11**, 111 (2015), doi:<https://doi.org/10.1038/nphys3224>.
- [5] D. Dell’Arciprete, M. L. Blow, A. T. Brown, F. D. C. Farrell, J. S. Lintuvuori, A. F. McVey, D. Marenduzzo and W. C. K. Poon, *A growing bacterial colony in two dimensions as an active nematic*, Nature Commun. **9**, 4190 (2018), doi:<https://doi.org/10.1038/s41467-018-06370-3>.
- [6] M. E. Cates, *Diffusive transport without detailed balance in motile bacteria: does microbiology need statistical physics?*, Rep. Prog. Phys. **75**, 042601 (2012), doi:<https://doi.org/10.1088/0034-4885/75/4/042601>.
- [7] S. Ramaswamy, *The mechanics and statistics of active matter*, Annu. Rev. Cond. Mat. Phys. **1**, 323 (2010), doi:<https://doi.org/10.1146/annurev-conmatphys-070909-104101>.
- [8] F. Jülicher, K. Kruse, J. Prost and J.-F. Joanny, *Active behavior of the cytoskeleton*, Physics Reports **449**, 3 (2007), doi:<https://doi.org/10.1016/j.physrep.2007.02.018>.
- [9] Y. Sumino, K. H. Nagai, Y. Shitaka, K. Yoshikawa, H. Chaté and K. Oiwa, *Large-scale vortex lattice emerging from collectively moving microtubules*, Nature **493**, 448 (2012), doi:<https://doi.org/10.1038/nature10874>.
- [10] F. J. Surrey, T. amd Nédélec, S. Leibler and E. Karsenti, *Physical properties determining self-organization of motors and microtubules*, Science **292**, 1167 (2001), doi:[10.1126/science.1059758](https://doi.org/10.1126/science.1059758).
- [11] T. Sanchez, D. T. N. Chen, S. J. DeCamp, M. Heymann and Z. Dogic, *Spontaneous motion in hierarchically assembled active matter*, Nature **491**, 431 (2012), doi:<https://doi.org/10.1038/nature11591>.
- [12] K. Kruse, J.-F. Joanny, F. Jülicher, J. Prost and K. Sekimoto, *Asters, vortices, and rotating spirals in active gels of polar filaments*, Phys. Rev. Lett. **92**, 078101 (2004), doi:<https://doi.org/10.1103/PhysRevLett.92.078101>.
- [13] H. H. Wensink, J. Dunkel, S. Heidenreich, K. Drescher, H. Lowen, R. E. Goldstein and J. M. Yeomans, *Meso-scale turbulence in living fluids*, Proc. Natl. Acad. Sci. USA **109**, 14308 (2012), doi:<https://doi.org/10.1073/pnas.1202032109>.
- [14] R. Alert, J. Casademunt and J. F. Joanny, *Active turbulence*, Annu. Rev. Cond. Mat. Phys. **13**, 143 (2022), doi:<https://doi.org/10.1146/annurev-conmatphys-082321-035957>.
- [15] S. M. Fielding, D. Marenduzzo and M. E. Cates, *Nonlinear dynamics and rheology of active fluids: Simulations in two dimensions*, Phys. Rev. E **83**, 041910 (2011), doi:<https://doi.org/10.1103/PhysRevE.83.041910>.

- [16] H. M. López, J. Gachelin, C. Douarche, H. Auradou and E. Clément, *Turning bacteria suspensions into superfluids*, Phys. Rev. Lett. **115**, 028301 (2015), doi:<https://doi.org/10.1103/PhysRevLett.115.028301>.
- [17] D. Saintillan, *Rheology of active fluids*, Annu. Rev. Fluid Mech. **50**, 563 (2018), doi:<https://doi.org/10.1146/annurev-fluid-010816-060049>.
- [18] J. Ignés-Mullol and F. Sagués, *Active, self-motile, and driven emulsions*, Curr. Op. Coll. & Interf. Sci. **49**, 16 (2020), doi:<https://doi.org/10.1016/j.cocis.2020.04.007>.
- [19] P. Guillamat, Z. Kos, J. Hardoüin, J. Ignés-Mullol, M. Ravnik and F. Sagués, *Active nematic emulsions*, Science Advances **4**, eaao1470 (2018), doi:[10.1126/sciadv.aao1470](https://doi.org/10.1126/sciadv.aao1470).
- [20] R. Sakamoto, Z. Izri, Y. Shimamoto and Y. T. Maeda, *Geometric trade-off between contractile force and viscous drag determines the actomyosin-based motility of a cell-sized droplet*, Proc. Natl. Acad. Sci. USA **119**, e2121147119 (2022), doi:<https://doi.org/10.1073/pnas.2121147119>.
- [21] L. Giomi and A. DeSimone, *Spontaneous division and motility in active nematic droplets*, Phys. Rev. Lett. **112**, 147802 (2014), doi:<https://doi.org/10.1103/PhysRevLett.112.147802>.
- [22] E. Tjhung, D. Marenduzzo and M. E. Cates, *Spontaneous symmetry breaking in active droplets provides a generic route to motility*, Proc. Nat. Acad. Sci., USA **109**, 12381 (2012), doi:<https://doi.org/10.1073/pnas.1200843109>.
- [23] E. Tjhung, A. Tiribocchi, D. Marenduzzo and M. E. Cates, *A minimal physical model captures the shapes of crawling cells*, Nature Commun. **6**, 5420 (2015), doi:[10.1038/ncomms6420](https://doi.org/10.1038/ncomms6420).
- [24] F. Ziebert and I. S. Aranson, *Computational approaches to substrate-based cell motility*, npj Comput. Mater. **2**, 16019 (2016), doi:<https://doi.org/10.1038/npjcompumats.2016.19>.
- [25] T. B. Saw, A. Doostmohammadi, V. Nier, L. Kocgozlu, S. Thampi, Y. Toyama, P. Marcq, C. T. Lim, J. M. Yeomans and B. Ladoux, *Topological defects in epithelia govern cell death and extrusion*, Nature **544**, 212 (2017), doi:<https://doi.org/10.1038/nature21718>.
- [26] L. A. Hoffmann, L. N. Carenza, J. Eckert and L. Giomi, *Theory of defect-mediated morphogenesis*, Science Advances **8**, eabk2712 (2022), doi:[10.1126/sciadv.abk2712](https://doi.org/10.1126/sciadv.abk2712).
- [27] M. Li, M. Brinkmann, I. Pagonabarraga, R. Seemann and J. P. Fleury, *Spatiotemporal control of cargo delivery performed by programmable self-propelled janus droplets*, Commun. Phys. **1**, 23 (2018), doi:<https://doi.org/10.1038/s42005-018-0025-4>.
- [28] C. Jin, Y. Chen, C. C. Maass and A. J. T. M. Mathijssen, *Collective entrainment and confinement amplify transport by schooling microswimmers*, Phys. Rev. Lett. **127**, 088006 (2021), doi:<https://doi.org/10.1103/PhysRevLett.127.088006>.
- [29] J. Wang and W. Gao, *Nano/microscale motors: biomedical opportunities and challenges*, ACS Nano **6**, 5745 (2012), doi:<https://doi.org/10.1021/nn3028997>.

- [30] W. Gao and J. Wang, *The environmental impact of micro/nanomachines: a review*, ACS Nano **8**, 3170 (2014), doi:<https://doi.org/10.1021/nm500077a>.
- [31] P. M. Davidson, J. Sliz, P. Isermann, C. Denais and J. Lammerding, *Design of a microfluidic device to quantify dynamic intra-nuclear deformation during cell migration through confining environments*, Integrative Biology **7**, 1534 (2015), doi:<https://doi.org/10.1039/c5ib00200a>.
- [32] K. M. Yamada and M. Sixt, *Mechanisms of 3d cell migration*, Nat. Rev. Mol. Cell Biol. **20**, 738 (2019), doi:<https://doi.org/10.1038/s41580-019-0172-9>.
- [33] B. V. Hokmabad, K. A. Baldwin, C. Krüger, C. Bahr and C. C. Maass, *Topological stabilization and dynamics of self-propelling nematic shells*, Phys. Rev. Lett. **123**, 178003 (2019), doi:<https://doi.org/10.1103/PhysRevLett.123.178003>.
- [34] B. V. Hokmabad, R. Dey, M. Jalaal, D. Mohanty, M. Almukambetova, K. A. Baldwin, D. Lohse and C. C. Maass, *Emergence of bimodal motility in active droplets*, Phys. Rev. X **11**, 011043 (2021), doi:<https://doi.org/10.1103/PhysRevX.11.011043>.
- [35] C. de Blois, M. Reyssat, S. Michelin and O. Dauchot, *Flow field around a confined active droplet*, Phys. Rev. Fluids **4**, 054001 (2019), doi:<https://doi.org/10.1103/PhysRevFluids.4.054001>.
- [36] C. Stamatopoulos, A. Milionis, N. Ackerl, M. Donati, P. L. de la Vallée, P. R. von Rohr and D. Poulikakos, *Droplet self-propulsion on superhydrophobic microtracks*, ACS Nano **14**, 12895 (2020), doi:<https://doi.org/10.1021/acsnano.0c03849>.
- [37] C. de Blois, V. Bertin, S. Saori, M. Ichikawa, M. Reyssat and O. Dauchot, *Swimming droplet in 1d geometries, an active bretherton problem*, Soft Matter **17**, 6646 (2021), doi:<https://doi.org/10.1039/D1SM00387A>.
- [38] E. Lauga and T. R. Powers, *The hydrodynamics of swimming microorganisms*, Rep. Prog. Phys **972**, 096601 (2009), doi:<https://doi.org/10.1088/0034-4885/72/9/096601>.
- [39] A. Zöttl and H. Stark, *Nonlinear dynamics of a microswimmer in poiseuille flow*, Phys. Rev. Lett. **108**, 218104 (2012), doi:<https://doi.org/10.1103/PhysRevLett.108.218104>.
- [40] B. Liu, K. S. Breuer and T. R. Powers, *Propulsion by a helical flagellum in a capillary tube*, Physics of Fluids **26**, 011701 (2014), doi:<https://doi.org/10.1063/1.4861026>.
- [41] A. Acemoglu and S. Yesilyurt, *Effects of geometric parameters on swimming of microorganisms with single helical flagellum in circular channels*, Biophys. Journ. **106**, 1537 (2014), doi:<https://doi.org/10.1016/j.bpj.2014.01.047>.
- [42] F. Fadda, G. Gonnella, A. Lamura and T. A., *Lattice boltzmann study of chemically-driven self-propelled droplets*, Eur. Phys. Journ. E **40**, 112 (2017), doi:<https://doi.org/10.1140/epje/i2017-11603-8>.
- [43] E. Kanso and S. Michelin, *Phoretic and hydrodynamic interactions of weakly confined autophoretic particles*, J. Chem. Phys. **150**, 044902 (2019), doi:<https://doi.org/10.1063/1.5065656>.

- [44] G.-J. Li and A. M. Ardekani, *Hydrodynamic interaction of microswimmers near a wall*, Phys. Rev. E **90**(1), 013010 (2014), doi:<https://doi.org/10.1103/PhysRevE.90.013010>.
- [45] J. S. Lintuvuori, A. T. Brown, K. Stratford and D. Marenduzzo, *Hydrodynamic oscillations and variable swimming speed in squirmers close to repulsive walls*, Soft Matter **12**(38), 7959 (2016), doi:<https://doi.org/10.1039/C6SM01353H>.
- [46] A. Doostmohammadi, J. Ignés-Mullol, J. M. Yeomans and F. Sagués, *Active nematics*, Nature Commun. **9**, 3246 (2018), doi:<https://doi.org/10.1038/s41467-018-05666-8>.
- [47] M. Fogliano, A. N. Morozov, O. Henrich and D. Marenduzzo, *Flow of deformable droplets: Discontinuous shear thinning and velocity oscillations*, Phys. Rev. Lett. **119**, 208002 (2017), doi:<https://doi.org/10.1103/PhysRevLett.119.208002>.
- [48] A. Tiribocchi, A. Montessori, M. Lauricella, F. Bonaccorso, S. Succi, S. Aime, M. Milani and D. Weitz, *The vortex-drive dynamics of droplets within droplets*, Nature Commun. **12**, 82 (2021), doi:<https://doi.org/10.1038/s41467-020-20364-0>.
- [49] P. G. de Gennes and J. Prost, *The physics of liquid crystals*, Oxford University Press, 2nd ed., ISBN: 9780198517856 (1993).
- [50] J. W. Cahn and J. E. Hilliard, *Free energy of a nonuniform system. i. interfacial free energy*, Jour. Chem. Phys. **28**, 258 (1958), doi:<https://doi.org/10.1063/1.1744102>.
- [51] A. J. Bray, *Theory of phase-ordering kinetics*, Advances in Physics **43**, 357 (1994), doi:<https://doi.org/10.1080/00018739400101505>.
- [52] L. N. Carenza, G. Gonnella, A. Lamura, G. Negro and A. Tiribocchi, *Lattice boltzmann methods and active fluids*, Eur. Phys. Jour. E **42**, 81 (2019), doi:<https://doi.org/10.1140/epje/i2019-11843-6>.
- [53] S. Succi, *The Lattice Boltzmann equation: For complex states of flowing matter*, Oxford University Press, doi:<https://doi.org/10.1093/oso/9780199592357.001.0001> (2018).
- [54] A. Tiribocchi, N. Stella, A. Lamura and G. Gonnella, *Hybrid lattice boltzmann model for binary fluid mixtures*, Phys. Rev. E **80**, 026701 (2009), doi:[10.1103/PhysRevE.80.026701](https://doi.org/10.1103/PhysRevE.80.026701).
- [55] S. Thampi, S. Ansumali, R. Adhikari and S. Succi, *Isotropic discrete laplacian operators from lattice hydrodynamics*, J. Comput. Phys. **234**, 1 (2013), doi:<https://doi.org/10.1016/j.jcp.2012.07.037>.
- [56] C. A. Whitfield, D. Marenduzzo, R. Voituriez and R. J. Hawkins, *Active polar fluid flow in finite droplets*, Eur. Phys. Jour. E **37**, 8 (2014), doi:<https://doi.org/10.1140/epje/i2014-14008-3>.
- [57] A. R. Fialho, M. R. Blow and D. Marenduzzo, *Anchoring-driven spontaneous rotations in active gel droplets*, Soft Matter **13**, 5933 (2017), doi:<https://doi.org/10.1039/C7SM01019B>.
- [58] E. Tjhung, D. Marenduzzo and M. E. Cates, *Contractile and chiral activities codetermine the helicity of swimming droplet trajectories*, Proc. Nat. Acad. Sci., USA **114**, 4631 (2017), doi:<https://doi.org/10.1073/pnas.1619960114>.